INTERNATIONAL JOURNAL FOR NUMERICAL AND ANALYTICAL METHODS IN GEOMECHANICS, VOL. 21, 133–149 (1997)

ELASTOPLASTIC ANALYSIS OF CYLINDRICAL CAVITY PROBLEMS IN GEOMATERIALS

PANOS PAPANASTASIOU[a] AND DAVID DURBAN[b]

[a]*Schlumberger Cambridge Research, Cambridge CB3 0EL, U.K.*
[b]*Faculty of Aerospace Engineering, Technion, Haifa 32000, Israel*

SUMMARY

A large-strain elastoplastic analysis is presented for a cylindrical cavity embedded in an infinite medium under uniform radial pressure. The investigation employs invariant, non-associated deformation-type theories for Mohr–Coulomb (M–C) and Drucker–Prager (D–P) solids, accounting for arbitrary hardening, with the equivalent stress as the independent variable. The M–C model results in a single first-order differential equation, whereas for the D–P solid an algebraic constraint supplements the governing differential equation. Material parameters and response characteristics were determined by calibrating the models with data from triaxial compression tests on Castlegate sandstone and on Jurassic shale. A comparison is presented between predictions obtained from the two models and experimental data from hollow cylinder tests under external loading. A sensitivity of the results to material parameters, like friction and dilation angles, is provided for the case of a cavity subjected to internal pressure in terms of limit pressure predictions. In all cases it has been found that the results of the D–P inner cone model are in close agreement with those obtained from the M–C model. © 1997 by John Wiley & Sons, Ltd.

Int. j. numer. methods geomech., vol. 21, 133–149 (1997)
(No. of Figures: 6 No. of Tables: 2 No. of Refs: 9)

Key words: cylindrical cavity; Mohr–Coulomb; Drucker–Prager

1. INTRODUCTION

The problem of cylindrical cavity expansion and contraction in an infinite medium is of significant interest in geotechnical, mining and petroleum industries. The analysis of an internally pressurized cavity is essential in interpreting pressuremeter and penetrometer tests and pile-driving phenomena in geotechnical engineering. On the other hand, the externally pressurized cavity can simulate the behaviour of mine shafts, tunnels and boreholes under remote hydrostatic stress-field.

Most of the existing analytical and semi-analytical work on cavity expansion[1–3] and cavity contraction[4] in pressure-sensitive geomaterials is based on elastic/perfectly plastic models and is restricted to the Mohr–Coulomb (M–C) solid. Collins and Stimpson[5] have recently studied the expansion of cylindrical and spherical cavities in hardening/softening soils, employing a rate constitutive relation, in conjunction with a self-similar numerical solution, to obtain the limit pressure.

Here, we present a complete large-strain study for axially symmetric plane-strain deformations of a cylindrical cavity, embedded in a pressure-sensitive elastoplastic solid. We analyse both problems of cavity expansion and contraction with Mohr–Coulomb (M–C) and Drucker–Prager

CCC 0363–9061/97/020133–17

Received 18 January 1996
Revised 28 July 1996

(D–P) solids. The models are based on deformation-type theories and can incorporate non-associativity with any form of strain hardening. The M–C model requires the numerical solution of a single first-order differential equation, whereas for the D–P model an algebraic constraint supplements the governing differential equation. The analysis provides the entire strain history of the pressurized cavity. It is worth noting that the simple solutions we obtain can be used for the validation of more complex numerical procedures, such as those based on the finite element method.

In Section 2, we present the M–C model and derive the solution for the cavity expansion field. The analysis centres on a deformation-type theory with the equivalent stress as the independent variable. The advantage of employing the deformation theory is that it facilitates the derivation of analytic and semi-analytic solutions, while with flow theory an incremental step-by-step numerical integration procedure should usually be followed. The use of deformation theories in elastoplastic problems is justified when the stress path does not deviate considerably from proportionality. Earlier studies[6, 7] have shown that in axially symmetric deformation patterns the loading path is nearly holonomic so that the standard flow theory may be replaced by the deformation theory. We elaborate the solution for the limit pressure and consider in particular the elastic/perfectly plastic material. Section 3 contains a similar analysis with the D–P model. The present theories are applied to the triaxial compression test in Section 4 in order to determine the material parameters of Castlegate sandstone for the M–C and D–P models. Sample numerical results are presented in Section 5. First, we simulate the hole closure of a thick-walled cylinder under external hydrostatic pressure and compare the theoretical results of the models with experimental data. Next, we show the elastoplastic response of an internally presurized cavity embedded in a Jurassic shale. Finally, we examine the sensitivity of the results to material parameters, like friction and dilation angles, in terms of limit pressure predictions of an internally pressurized cavity. Predictions with the M–C and D–P inner cone models were found to be in close agreement for all cases examined in this study.

2. MOHR–COULOMB ANALYSIS

We consider a circular cylindrical cavity embedded in a pressure-sensitive elastoplastic medium and subjected to monotonically increasing internal pressure p. For a plane-strain axially symmetric deformation pattern we expect, with the usual notation, the following ordering of stresses:

$$\sigma_r < \sigma_z < \sigma_\theta \tag{1}$$

For the M–C constitutive model we define the plastic potential $\bar{\phi}$ and equivalent stress $\bar{\sigma}_e$:

$$\bar{\phi} = \bar{\eta}\sigma_\theta - \sigma_r, \quad \bar{\sigma}_e = \bar{\mu}\sigma_\theta - \sigma_r \tag{2a, b}$$

where $(\bar{\eta}, \bar{\mu})$ are material parameters, determined from the calibration procedure explained in Section 4. Particular cases are the associated behaviour which is obtained when $\bar{\eta} = \bar{\mu}$ and the Tresca solid with $\bar{\eta} = \bar{\mu} = 1$.

The plastic strain rates are derived from the normality condition

$$\dot{\varepsilon}_r^p = \Lambda \frac{\partial \bar{\phi}}{\partial \sigma_r} = -\Lambda, \quad \dot{\varepsilon}_\theta^p = \Lambda \frac{\partial \bar{\phi}}{\partial \sigma_\theta} = \Lambda\bar{\eta}, \quad \dot{\varepsilon}_z^p = 0 \tag{3}$$

where Λ is the plastic multiplier. The principle of plastic power equivalence implies that

$$\sigma_r\dot{\varepsilon}_r^p + \sigma_\theta\dot{\varepsilon}_\theta^p = \bar{\sigma}_e\dot{\bar{\varepsilon}}_p \tag{4}$$

where the equivalent plastic strain $\bar{\varepsilon}_p$ is a known function of the equivalent stress $\bar{\sigma}_e$. Combining (3) and (4) results in

$$\Lambda = \frac{\bar{\sigma}_e}{\bar{\phi}} \dot{\bar{\varepsilon}}_p \tag{5}$$

and the plastic strain rates from equation (3) become

$$\dot{\varepsilon}_r^p = -\frac{\bar{\sigma}_e}{\bar{\phi}} \dot{\bar{\varepsilon}}_p, \quad \dot{\varepsilon}_\theta^p = -\bar{\eta} \frac{\bar{\sigma}_e}{\bar{\phi}} \dot{\bar{\varepsilon}}_p \tag{6}$$

We assume that the elastic branch of the constitutive relations obeys Hooke's law, to arrive at the standard rate formulation

$$\dot{\varepsilon}_r = \frac{1}{E}[\dot{\sigma}_r - \nu(\dot{\sigma}_\theta + \dot{\sigma}_z)] - \frac{\bar{\sigma}_e}{\bar{\phi}} \dot{\bar{\varepsilon}}_p \tag{7a}$$

$$\dot{\varepsilon}_\theta = \frac{1}{E}[\dot{\sigma}_\theta - \nu(\dot{\sigma}_z + \dot{\sigma}_r)] + \bar{\eta} \frac{\bar{\sigma}_e}{\bar{\phi}} \dot{\bar{\varepsilon}}_p \tag{7b}$$

$$\dot{\varepsilon}_z = \frac{1}{E}[\dot{\sigma}_z - \nu(\dot{\sigma}_r + \dot{\sigma}_\theta)] \tag{7c}$$

where (E, ν) and Young's modulus and Poisson's ratio, respectively. In plane strain, however, $\dot{\varepsilon}_z = 0$ and (7c) implies

$$\dot{\sigma}_z = \nu(\dot{\sigma}_r + \dot{\sigma}_\theta) \tag{8}$$

or, after integrating (taking into account the initial hydrostatic stress $\sigma_r = \sigma_\theta = \sigma_z = -p_0$),

$$\sigma_z = \nu(\sigma_r + \sigma_\theta) - (1 - 2\nu)p_0 \tag{9}$$

Next, we eliminate the axial stress rate $\dot{\sigma}_z$ between (7a) and (7b), with the aid of (8), to get the plane-strain constitutive relations

$$\begin{aligned} \dot{\varepsilon}_r &= \frac{1}{E}[(1 - \nu^2)\dot{\sigma}_r - \nu(1 + \nu)\dot{\sigma}_\theta] - \frac{\dot{\sigma}_e}{\bar{\phi}} \dot{\bar{\varepsilon}}_p \\ \dot{\varepsilon}_\theta &= \frac{1}{E}[-\nu(1 + \nu^2)\dot{\sigma}_r + (1 - \nu^2)\dot{\sigma}_\theta] + \bar{\eta} \frac{\dot{\sigma}_e}{\bar{\phi}} \dot{\bar{\varepsilon}}_p \end{aligned} \tag{10}$$

For the associated M–C model $\bar{\sigma}_e = \bar{\phi}$ so that relations (10) are holonomic and can be exactly integrated along the loading history. For the non-associated case, one may expect little deviations from the proportional path in the stress space and proceed with the deformation-type theory whereby (10) is replaced by the finite strain versions

$$\varepsilon_r = (1 - \nu^2)\Sigma_r - \nu(1 + \nu)\Sigma_\theta - \frac{\bar{\Sigma}}{\bar{\Phi}} \bar{\varepsilon}_p + (1 + \nu)(1 - 2\nu)P_0 \tag{11a}$$

$$\varepsilon_\theta = -\nu(1 + \nu)\Sigma_r + (1 - \nu^2)\Sigma_\theta + \bar{\eta} \frac{\bar{\Sigma}}{\bar{\Phi}} \bar{\varepsilon}_p + (1 + \nu)(1 - 2\nu)P_0 \tag{11b}$$

Here, we have introduced the non-dimensionalized notation

$$\Sigma_r = \frac{\sigma_r}{E}, \quad \Sigma_\theta = \frac{\sigma_\theta}{E}, \quad \Sigma_z = \frac{\sigma_z}{E}, \quad \bar{\Sigma} = \frac{\bar{\sigma}_e}{E}, \quad \bar{\Phi} = \frac{\bar{\phi}}{E}, \quad P_0 = \frac{p_0}{R} \tag{12}$$

and $\bar{\varepsilon}_p$ is understood to be a known function of $\bar{\Sigma}$ as determined by the calibration procedure. Likewise, we write the axial relation (9) as

$$\Sigma_z = \nu(\Sigma_r + \Sigma_\theta) - (1 - 2\nu)P_0 \tag{13}$$

Denoting by r the original undeformed radius, and by u the radial displacement, we have the finite strain components

$$\varepsilon_r = \ln\left(1 + \frac{du}{dr}\right), \quad \varepsilon_\theta = \ln\left(1 + \frac{u}{r}\right) \tag{14a, b}$$

which are combined to produce the compatibility condition

$$d\varepsilon_\theta = (e^{\varepsilon_r - \varepsilon_\theta} - 1)\frac{dr}{r} \tag{15}$$

Stress equilibrium in the radial direction requires that

$$\frac{d\sigma_r}{d(r+u)} + \frac{\sigma_r - \sigma_\theta}{r+u} = 0 \tag{16}$$

or with the aid of (14) and (12),

$$d\Sigma_r = (\Sigma_\theta - \Sigma_r)e^{\varepsilon_r - \varepsilon_\theta}\frac{dr}{r} \tag{17}$$

Now, we eliminate the radial co-ordinate between (15) and (17), and take the equivalent stress $\bar{\Sigma}$ as the independent variable to obtain

$$(1 - e^{\varepsilon_\theta - \varepsilon_r})\Sigma_r' - (\Sigma_\theta - \Sigma_r)\varepsilon_\theta' = 0 \tag{18}$$

where the prime denotes differentiation with respect to $\bar{\Sigma}$. Equation (18) can be further reduces to a single ODE for Σ_r in terms of $\bar{\Sigma}$. This can be done using the identities, by (2),

$$\Sigma_\theta - \Sigma_r = \frac{1}{\bar{\mu}}[\bar{\Sigma} + (1 - \bar{\mu})\Sigma_r] \tag{19}$$

$$\bar{\Phi} = \frac{1}{\bar{\mu}}[\bar{\eta}\bar{\Sigma} + (\bar{\eta} - \bar{\mu})\Sigma_r] \tag{20}$$

From (11) it follows that

$$\varepsilon_\theta - \varepsilon_r = \frac{1+\nu}{\bar{\mu}}[\bar{\Sigma} + (1 - \bar{\mu})\Sigma_r] + (1 + \bar{\eta})\frac{\bar{\Sigma}}{\bar{\Phi}}\bar{\varepsilon}_p \tag{21}$$

is a known function $(\bar{\Sigma}, \Sigma_r)$. Similarly, the circumferential strain component (11b) can be put in the form

$$\varepsilon_\theta = (1 + \nu)\left[\frac{1-\nu}{\bar{\mu}}\bar{\Sigma} + \left(\frac{1-\nu}{\bar{\mu}} - \nu\right)\Sigma_r\right] + \bar{\eta}\frac{\bar{\Sigma}}{\bar{\Phi}}\bar{\varepsilon}_p + (1 + \nu)(1 - 2\nu)P_0 \tag{22}$$

Finally, inserting the derivative ε_θ' from (22) in (18), along with (19) and (21), we arrive at the governing equation

$$\Sigma_r' = -F(\bar{\Sigma}, \Sigma_r) = -\frac{A\ \ B}{C-1+A\ \ D} \tag{23}$$

with

$$\begin{aligned} A &= \bar{\Sigma} + (1-\bar{\mu})\Sigma_r \\ B &= \alpha_1 + \beta_1 \frac{\bar{\Sigma}}{\bar{\Phi}} \bar{\varepsilon}_{\mathrm{p}}' + \beta_2 \frac{\Sigma_r}{\bar{\Phi}^2} \bar{\varepsilon}_{\mathrm{p}} \\ C &= \exp\left\{\alpha_3[\bar{\Sigma} + (1-\bar{\mu})\Sigma_r] + (1+\bar{\eta})\frac{\bar{\Sigma}}{\bar{\Phi}} \bar{\varepsilon}_{\mathrm{p}}\right\} \\ D &= \alpha_2 - \beta_2 \frac{\bar{\Sigma}}{\bar{\Phi}^2} \bar{\varepsilon}_{\mathrm{p}} \end{aligned} \tag{24}$$

where

$$\begin{aligned} &\alpha_1 = \frac{1-\nu^2}{\bar{\mu}^2}, \quad \alpha_2 = \frac{1+\bar{\nu}}{\bar{\mu}^2}(1-\nu-\nu\bar{\mu}) \\ &\alpha_3 = \frac{1+\nu}{\bar{\mu}}, \quad \beta_1 = \frac{\bar{\eta}}{\bar{\mu}}, \quad \beta_2 = \frac{\bar{\eta}(\bar{\eta}-\bar{\mu})}{\bar{\mu}^2} \end{aligned} \tag{25}$$

A second equation is obtained from (17) and (23), using (19) and (21), viz.

$$\ln' r = -G(\bar{\Sigma}, \Sigma_r) = \frac{\bar{\mu}C}{A} F(\bar{\Sigma}, \Sigma_r) \tag{26}$$

The governing equations, (23) and (26), are supplemented with the boundary conditions

$$\begin{aligned} \Sigma_r &= -P \quad \text{at } r = a \\ \Sigma_r &= -P_0 \quad \text{at } r = b \end{aligned} \tag{27}$$

where (a, b) are the inner and outer underformed radii, respectively, and $P = p/E$ is the non-dimensionalized inner pressure. The independent variable here is the equivalent stress $\bar{\Sigma}$ and a standard integration routine would begin from the known value $\bar{\Sigma} = \bar{\Sigma}_b$ at $r = b$ and stopped at the given pressure P at $r = a$. Repeated integrations with increasing values of $\bar{\Sigma}_b$ will determine the entire loading history. The circumferential stress component is then obtained from (19) and the spatial stress profiles, with respect to the deformed radial coordinate ($R = r + u$), are provided by the transformation

$$\ln \frac{R}{r} = \bar{\mu}(\alpha_1 \bar{\Sigma} + \alpha_2 \Sigma_r) + \bar{\eta} \frac{\bar{\Sigma}}{\bar{\Phi}} \bar{\varepsilon}_{\mathrm{p}} + (1+\nu)(1-2\nu)P_0 \tag{28}$$

which follows from (22) and (14b).

Although a definite yield point has not been introduced so far there is no difficulty in implementing elastic/plastic response characteristics that exhibit a definite yield point and activate the plastic branch of (10) and (11) at any stage of the loading process. For the deformation patterns considered here initial yield will occur at the cavity and a plastic zone will

spread radially outwards with increasing load. The remote elastic field can be well approximated by the small-strain elastic solution

$$\Sigma_r = -P_\infty - H/r^2, \quad \Sigma_\theta = -P_\infty + H/r^2, \quad \Sigma_z = -2\nu P_\infty - (1-2\nu)P_0 \tag{29}$$

where P_∞ is the applied isotropic pressure at infinity and H is a constant. For the internally pressurized cavity, $P_\infty = P_0$ and the equivalent stress from (2b) is

$$\bar{\Sigma} = (1-\bar{\mu})P_0 + (1+\bar{\mu})H/r^2 \tag{30}$$

The constant H can be eliminated from (29) and (30), resulting in

$$\Sigma_r = -\frac{\bar{\Sigma} + 2\bar{\mu}P_0}{1+\bar{\mu}}, \quad \Sigma_\theta = \frac{\bar{\Sigma} - 2P_0}{1+\bar{\mu}} \tag{31}$$

At the elastoplastic interface $\bar{\Sigma} = \bar{Y}/E = \bar{\Sigma}_Y$ ($\bar{Y}$ being the initial yield stress) and the first of (31) provides the expression for the radial stress

$$\Sigma_r = -\frac{\bar{\Sigma}_Y + 2\bar{\mu}P_0}{1+\bar{\mu}} \quad \text{at } \bar{\Sigma} = \bar{\Sigma}_Y \tag{32}$$

Equation (23) can now be integrated in the entire domain to produce the universal loading history in the $(\bar{\Sigma}, \Sigma_r)$ plane. Notice also that the equivalent plastic strain $\bar{\varepsilon}_p$ remains identically zero as long as $\bar{\Sigma} \leqslant \bar{\Sigma}_Y$.

For an externally pressurized cavity, the ordering of stresses is $\sigma_\theta < \sigma_z < \sigma_r$ and the solution can be obtained along the same lines by interchanging the stresses σ_r, σ_θ in the definitions of plastic potential and equivalent stress in (2). In fact, the similarity between the expansion and contraction deformation patterns allows us to obtain the governing equations for the cavity contraction problem from (23)–(26) by using the transformation

$$\bar{\eta} \to \frac{1}{\bar{\eta}}, \quad \bar{\mu} \to \frac{1}{\bar{\mu}}, \quad \bar{\phi} \to -\frac{\bar{\phi}}{\bar{\eta}}, \quad \bar{\varepsilon}_p \to -\bar{\mu}\bar{\varepsilon}_p \tag{33}$$

A useful, though less realistic, material response is provided by the elastic/perfectly plastic model. In that case, a similar analysis can be performed but with the equivalent plastic strain $\bar{\varepsilon}_p$ as the independent variable instead of the equivalent stress $\bar{\Sigma}$ (which is now a constant, $\bar{\Sigma}_Y$). The spatial (Eulerian) stress profiles in the plastic zone can be determined, for both theories, from the yield condition and the equilibrium equation. Just to provide an example, for the expanding cavity we find the radial stress profile

$$\Sigma_r = \frac{\bar{\Sigma}_Y}{\bar{\mu}-1} - \left(P + \frac{\bar{\Sigma}_Y}{\bar{\mu}-1}\right)\left(\frac{R_a}{R}\right)^{(\bar{\mu}-1)/\bar{\mu}} \tag{34}$$

with a similar expression for Σ_θ. Compliance with the elastic/plastic interface conditions and using the fact, by (10), that $(\bar{\eta}\varepsilon_r + \varepsilon_\theta)$ is holonomic completes the analysis. It has been shown by Durban and Fleck[8] that the stress field is identical for both flow and deformation theories.

3. DRUCKER–PRAGER ANALYSIS

The Drucker–Prager[9] model (D–P) can be understood as an extension of the von Mises model for pressure-sensitive materials such as soil and rocks. It can also be considered as the first attempt to approximate the well-known M–C criterion by a simple smooth function. The D–P model, as

recently modified by Durban and Fleck,[8] employs the plastic potential ϕ and equivalent stress σ_e,

$$\phi = (\tfrac{3}{2}\mathbf{S}\cdot\cdot\mathbf{S})^{1/2} + \tfrac{1}{3}\eta\mathbf{I}\cdot\cdot\boldsymbol{\sigma}, \quad \sigma_e = (\tfrac{3}{2}\mathbf{S}\cdot\cdot\mathbf{S})^{1/2} + \tfrac{1}{3}\mu\mathbf{I}\cdot\cdot\boldsymbol{\sigma} \tag{35a, b}$$

where $\boldsymbol{\sigma}$ is the Cauchy stress tensor, $\mathbf{S}$ is its deviator, $\mathbf{I}$ is the unit tensor and (η, μ) are material parameters (defined differently from those in the Mohr–Coulomb model). Associated plasticity is recovered for $\eta = \mu$ and the von Mises material model is obtained with $\eta = \mu = 0$.

The plastic strain rate tensor is generated from the normality condition and plastic power equivalence,[8]

$$\mathbf{D}^p = \frac{\sigma_e}{\phi}\dot{\varepsilon}_p\,[(\tfrac{3}{2}\mathbf{S}\cdot\cdot\mathbf{S})^{-1/2}(\tfrac{3}{2}\mathbf{S}) + \tfrac{1}{3}\eta\mathbf{I}] \tag{36}$$

where the equivalent plastic strain ε_p is a given function of the equivalent stress σ_e in (35b).

Following a procedure similar to that for the Mohr–Coulomb model, the deformation theory relations for the Drucker–Prager model are

$$\varepsilon_r = \Sigma_r - \nu(\Sigma_\theta + \Sigma_r) + \frac{\Sigma}{\Phi}\varepsilon_p\left[\frac{3(\Sigma_r - \Sigma_h)/2}{\Sigma - \mu\Sigma_h} + \frac{1}{3}\eta\right] + (1-2\nu)P_0 \tag{37a}$$

$$\varepsilon_\theta = \Sigma_\theta - \nu(\Sigma_z + \Sigma_r) + \frac{\Sigma}{\Phi}\varepsilon_p\left[\frac{3(\Sigma_\theta - \Sigma_h)/2}{\Sigma - \mu\Sigma_h} + \frac{1}{3}\eta\right] + (1-2\nu)P_0 \tag{37b}$$

$$\varepsilon_z = \Sigma_z - \nu(\Sigma_r + \Sigma_\theta) + \frac{\Sigma}{\Phi}\varepsilon_p\left[\frac{3(\Sigma_z - \Sigma_h)/2}{\Sigma - \mu\Sigma_h} + \frac{1}{3}\eta\right] + (1-2\nu)P_0 = 0 \tag{37c}$$

where $\Sigma_h = (\boldsymbol{\Sigma}\cdot\cdot\mathbf{I})/3$ is the dimensionless hydrostatic stress, $\boldsymbol{\Sigma} = \boldsymbol{\sigma}/E$, and we note the relation

$$\Sigma_e - \mu\Sigma_h = \sqrt{\tfrac{3}{2}}[(\Sigma_r - \Sigma_h)^2 + (\Sigma_\theta - \Sigma_h)^2 + (\Sigma_z - \Sigma_h)^2]^{1/2} \tag{38}$$

In plane-strain deformation $\varepsilon_z = 0$ and (37c) can then be solved for Σ_z in terms of Σ and Σ_h. To this end we employ the simple identity $\Sigma_r + \Sigma_\theta = 3\Sigma_h - \Sigma_z$ and insert it in (37c) to obtain

$$\Sigma_z = \frac{[6\nu\Phi\Sigma_h - 2\eta\Sigma\varepsilon_p/3 - 2(1-2\nu)\Phi P_0](\Sigma - \mu\Sigma_h) + 3\Sigma_h\Sigma\varepsilon_p}{2(1+\nu)\Phi(\Sigma - \mu\Sigma_h) + 3\Sigma\varepsilon_p} \tag{39}$$

where from (35)

$$\Phi = \Sigma + (\eta - \mu)\Sigma_h \tag{40}$$

Next, we solve (37c) with (39) for

$$\Sigma_r + \Sigma_\theta = \frac{[6\Phi\Sigma_h + 2\eta\Sigma\varepsilon_p/3 + 2(1-2\nu)\Phi P_0](\Sigma - \mu\Sigma_h) + 6\Sigma_h\Sigma\varepsilon_p}{2(1+\nu)\Phi(\Sigma - \mu\Sigma_h) + 3\Sigma\varepsilon_p} \tag{41}$$

Equation (38) can be written as

$$(\Sigma_\theta - \Sigma_r)^2 = 4(\Sigma - \mu\Sigma_h)^2/3 - 3(\Sigma_z - \Sigma_h)^2 \tag{42}$$

Combining this with (39) gives the stress difference $(\Sigma_\theta - \Sigma_r)$ in terms of (Σ, Σ_h), namely

$$\Sigma_\theta - \Sigma_r = m(\Sigma - \mu\Sigma_h)\left\{\frac{4}{3} - 3\left[\frac{2(1-2\nu)\Phi(\Sigma_h + P_0) + 2\eta\Sigma\varepsilon_p/3}{2(1+\nu)\Phi(\Sigma - \mu\Sigma_h) + 3\Sigma\varepsilon_p}\right]^2\right\}^{1/2} \tag{43}$$

where $m = \operatorname{sgn}\{\Sigma_\theta - \Sigma_r\}$. For the internally pressurized cavity $m = 1$, while for the contracting cavity $m = -1$. Notice that all three stress components are expressible as algebraic functions of the equivalent stress Σ and the hydrostatic stress Σ_h. The axial component is given by (39) while Σ_r and Σ_θ follow from (41) and (43).

Turning now to the equilibrium (17) and compatibility (15) requirements we have, from (37a) and (37b), the relation

$$\varepsilon_r - \varepsilon_\theta = -\left[(1+\nu) + \frac{3\Sigma\varepsilon_p}{2\Phi(\Sigma - \mu\Sigma_h)}\right](\Sigma_\theta - \Sigma_r) \tag{44}$$

which is an explicit function of (Σ, Σ_h) by (43). Similarly, equation (37b) can be written again as an explicit function of (Σ, Σ_h),

$$\varepsilon_\theta = \left[(1+\nu) + \frac{3\Sigma\varepsilon_p}{2\Phi(\Sigma - \mu\Sigma_h)}\right](\Sigma_\theta - \Sigma_h) + \frac{\eta\Sigma\varepsilon_p}{3\Phi} + (1-2\nu)(\Sigma_h + P_0) \tag{45}$$

In order to facilitate the integration of (18) we rewrite the $(\Sigma_\theta - \Sigma_h)$ term in (45) as

$$\Sigma_\theta - \Sigma_h = L_1 - \Sigma_r \tag{46}$$

where $L_1 = (\Sigma_r + \Sigma_\theta) - \Sigma_h$ is a known function of (Σ, Σ_h) by (41). Also, the differential form of ε_θ from (45) is written as

$$\mathrm{d}\varepsilon_\theta = \frac{\partial\varepsilon_\theta}{\partial\Sigma}\,\mathrm{d}\Sigma + \frac{\partial\varepsilon_\theta}{\partial\Sigma_h}\,\mathrm{d}\Sigma_h + \frac{\partial\varepsilon_\theta}{\partial\Sigma_r}\,\mathrm{d}\Sigma_r \tag{47}$$

Substituting this in (18) gives the governing equation

$$\left[1 - \mathrm{e}^{\varepsilon_\theta - \varepsilon_r} - (\Sigma_\theta - \Sigma_r)\frac{\partial\varepsilon_\theta}{\partial\Sigma_r}\right]\frac{\mathrm{d}\Sigma_r}{\mathrm{d}\Sigma} - (\Sigma_\theta - \Sigma_r)\frac{\partial\varepsilon_\theta}{\partial\Sigma_h}\frac{\mathrm{d}\Sigma_h}{\mathrm{d}\Sigma} = (\Sigma_\theta - \Sigma_r)\frac{\partial\varepsilon_\theta}{\partial\Sigma} \tag{48}$$

This equation can be solved in conjunction with the expression for Σ_r obtained by combining (41) and (43). The partial derivatives of ε_θ in (48) are explicit functions of (Σ, Σ_h) and can be evaluated without difficulty from (45) for any hardening characteristic, viz.

$$\begin{aligned}
\frac{\partial\varepsilon_\theta}{\partial\Sigma_r} &= -\left[(1+\nu) + \frac{3\Sigma\varepsilon_p}{2\Phi(\Sigma - \mu\Sigma_h)}\right] \\
\frac{\partial\varepsilon_\theta}{\partial\Sigma_h} &= -\frac{(\eta - 2\mu)\Sigma - 2\mu(\eta - \mu)\Sigma_h}{(\Sigma - \mu\Sigma_h)^2}\left(\frac{3\Sigma\varepsilon_p}{2\Phi^2}\right)\Sigma_r + 3(1-\nu) \\
&\quad + \frac{3\Sigma^2\varepsilon_p}{2\Phi(\Sigma - \mu\Sigma_h)^2} - (\eta - \mu)\left[\frac{3\Sigma_h}{2(\Sigma - \mu\Sigma_h)} + \frac{2}{3}\eta\right]\frac{\Sigma\varepsilon_p}{\Phi^2} \\
\frac{\partial\varepsilon_\theta}{\partial\Sigma} &= \frac{3(\Sigma_r - \Sigma_h)}{2(\Sigma - \mu\Sigma_h)^2}\left(\frac{\Sigma\varepsilon_p}{\Phi}\right) - \left[\frac{3(\Sigma_r - \Sigma_h)}{2(\Sigma - \mu\Sigma_h)} - \frac{2}{3}\eta\right]\left(\frac{\Sigma}{\Phi}\,\varepsilon_p' + \frac{(\eta - \mu)\Sigma_h}{\Phi^2}\right)
\end{aligned} \tag{49}$$

To further simplify the analysis let us introduce the notation

$$L_2 = \Sigma_r + \Sigma_\theta, \quad L_3 = \Sigma_\theta - \Sigma_r, \quad \Sigma_r = (L_2 - L_3)/2 \tag{50}$$

and, by (44),

$$\varepsilon_\theta - \varepsilon_r = \left[(1+\nu) + \frac{3\Sigma\varepsilon_p}{2\Phi(\Sigma - \mu\Sigma_h)}\right]L_3 = L_4 \tag{51}$$

which defines L_4. The governing equation (48) is now

$$\left[1 - e^{L_4} - L_3 \frac{\partial \varepsilon_\theta}{\partial \Sigma_r}\right] \frac{d\Sigma_r}{d\Sigma} - L_3 \frac{\partial \varepsilon_\theta}{\partial \Sigma_h} \frac{d\Sigma_h}{d\Sigma} = L_3 \frac{\partial \varepsilon_\theta}{\partial \Sigma} \tag{52}$$

with Σ_r given in (50).

Once the variation of Σ_r and Σ_h with Σ has been determined we can find the radial profiles by integrating (17) in the form

$$\frac{dr}{r} = \frac{e^{L_4}}{L_3} d\Sigma_r \tag{53}$$

The stress components $(\Sigma_\theta, \Sigma_z)$ are easily evaluated from (39) and (41) and the radial displacement is found from (45).

The remote small-strain elastic field is given by (29) along with the hydrostatic stress

$$\Sigma_h = -\tfrac{2}{3}(1+\nu)P_\infty - \tfrac{1}{3}(1-2\nu)P_0 \tag{54}$$

The D–P equivalent stress follows as

$$\Sigma = \left[(1-2\nu)^2(P_\infty - P_0)^2 + 3\left(\frac{H}{r^2}\right)^2\right]^{1/2} - \mu\left[\tfrac{2}{3}(1+\nu)P_\infty + \tfrac{1}{3}(1-2\nu)P_0\right] \tag{55}$$

and for the internally pressurized cavity, with $P_\infty = P_0$, this is reduced to

$$\Sigma = \sqrt{3}\frac{H}{r^2} - \mu P_0 \tag{56}$$

and the stress components become accordingly

$$\Sigma_r = -\frac{\Sigma + (\mu + \sqrt{3})}{\sqrt{3}}, \quad \Sigma_\theta = \frac{\Sigma + (\mu - \sqrt{3})}{\sqrt{3}}, \quad \Sigma_z = \Sigma_h = -P_0 \tag{57}$$

For a cavity under increasing external pressure ($P_\infty = P$) or decreasing internal pressure ($P_\infty = P_0$), the state of stress can be obtained from (57) using the transformation $(r, \theta) \to (\theta, r)$.

4. MODELS CALIBRATION

The material parameters and response characteristics of the constitutive models are determined by calibration procedure of experimental data from triaxial compression tests. Typically, in these tests a cylindrical specimen is subjected to hydrostatic pressure p_0 which is followed by increasing the load in the axial direction. Denoting the principal axes by (1, 2, 3), the loading path follows as

$$\sigma_1 = -\sigma, \quad \sigma_2 = \sigma_3 = -p_0 \tag{58}$$

where $\sigma > p_0$ is the current level of axial compression.

For the M–C solid the plastic potential and equivalent stress are given by

$$\bar{\phi} = \sigma - \bar{\eta} p_0, \quad \bar{\sigma}_e = \sigma - \bar{\mu} p_0 \tag{59}$$

and the strain rates follow as

$$\dot{\varepsilon}_1 = -\frac{\dot{\sigma}}{E} - \frac{\bar{\sigma}_e}{\bar{\phi}} \dot{\bar{\varepsilon}}_p, \quad \dot{\varepsilon}_2 = \dot{\varepsilon}_3 = \frac{\nu \dot{\sigma}}{E} + \left(\frac{\bar{\eta}}{2}\right) \frac{\bar{\sigma}_e}{\bar{\phi}} \dot{\bar{\varepsilon}}_p \tag{60}$$

The value of parameter $\bar{\mu}$ can be determined from the slope of the initial yield envelope while the value of $\bar{\eta}$ can be obtained from the plastic contraction ratio which is equal to $\bar{\eta}/2$. The corresponding hardening function, $\bar{\varepsilon}_{\mathrm{p}} = \bar{\varepsilon}_{\mathrm{p}}(\bar{\sigma}_{\mathrm{e}})$, is obtained by fitting (60) to experimental data.

For the D–P model we obtain the following relations for the plastic potential and equivalent stress

$$\phi = (1 - \tfrac{1}{3}\eta)\sigma - (1 + \tfrac{2}{3}\eta)p_0, \quad \sigma_{\mathrm{e}} = (1 - \tfrac{1}{3}\mu)\sigma - (1 + \tfrac{2}{3}\mu)p_0 \tag{61}$$

along with the strain rates

$$\dot{\varepsilon}_1 = -\frac{\dot{\sigma}}{E} - (1 - \tfrac{1}{3}\eta)\frac{\sigma_{\mathrm{e}}}{\phi}\dot{\varepsilon}_{\mathrm{p}}, \quad \dot{\varepsilon}_2 = \dot{\varepsilon}_3 = \frac{v\dot{\sigma}}{R} + (\tfrac{1}{2} + \tfrac{1}{3}\eta)\frac{\sigma_{\mathrm{e}}}{\phi}\dot{\varepsilon}_{\mathrm{p}} \tag{62}$$

It is reasonable to require that both models predicts an identical loading history for the triaxial compression test. This leads to some interesting observations with regard to the plastic parameters. Equating the plastic parts of (60) and (62) gives

$$\bar{\eta} = \frac{1 + \frac{2}{3}\eta}{1 - \frac{1}{3}\eta} \;\Leftrightarrow\; \eta = \frac{3(\bar{\eta} - 1)}{\bar{\eta} + 2} \tag{63}$$

Relations (63) imply an identical slope for the potential lines $\bar{\phi}$ and ϕ of (59) and (61).

Also, by requiring the initial yield lines ($\bar{\sigma}_{\mathrm{e}} = \bar{Y}$ and $\bar{\sigma}_{\mathrm{e}} = Y$) from (59) and (61) to be identical in the (σ, p_0) plane we find

$$\bar{\mu} = \frac{1 + \frac{2}{3}\mu}{1 - \frac{1}{3}\mu} \;\Leftrightarrow\; \mu = \frac{3(\bar{\mu} - 1)}{\bar{\mu} + 2} \tag{64}$$

which are similar to (63). Furthermore, it is well known that the M–C parameters are related to the dilation angle ψ and the internal friction angle φ by

$$\bar{\eta} = \frac{1 + \sin\psi}{1 - \sin\psi}, \quad \bar{\mu} = \frac{1 + \sin\varphi}{1 - \sin\varphi} \tag{65}$$

Equations (63)–(65) give for the D–P solid

$$\eta = \frac{6\sin\psi}{3 - \sin\psi}, \quad \mu = \frac{6\sin\phi}{3 - \sin\phi} \tag{66}$$

Substituting $\bar{\eta}$ and $\bar{\mu}$ from (63) and (64) in (59), and noting (61) results in the transformations

$$\phi = (1 - \tfrac{1}{3}\eta)\bar{\phi}, \quad \sigma_{\mathrm{e}} = (1 - \tfrac{1}{3}\mu)\bar{\sigma}_{\mathrm{e}} \tag{67}$$

which are further combined with the plastic parts of (60) and (62) to give

$$\dot{\varepsilon}_{\mathrm{p}} = \frac{\dot{\bar{\varepsilon}}_{\mathrm{p}}}{1 - \frac{1}{3}\mu} \;\Rightarrow\; \varepsilon_{\mathrm{p}} = \frac{\bar{\varepsilon}_{\mathrm{p}}}{1 - \frac{1}{2}\mu} \tag{68}$$

These transformations enable us to correlate the material parameters of each model in the triaxial compression test. As an example, we consider the M–C stress–strain hardening response

$$\bar{\varepsilon}_{\mathrm{p}} = \bar{K}(\bar{\sigma}_{\mathrm{e}} - \bar{Y})^n, \quad \bar{\sigma}_{\mathrm{e}} \geqslant \bar{Y} \tag{69}$$

This can be easily transformed into the D–P relation

$$\varepsilon_{\mathrm{p}} = K(\sigma_{\mathrm{e}} - Y)^n, \quad \sigma_{\mathrm{e}} \geqslant Y \tag{70}$$

where

$$K = \frac{\bar{K}}{(1 - \frac{1}{3}\mu)^{n+1}}, \quad Y = (1 - \tfrac{1}{3}\mu)\bar{Y} \tag{71}$$

The set of transformations derived here from the M–C model to the D–P model can be constructed from a different point of view. Indeed, if the D–P cones (of plastic potential and yield surface) are made to coincide in the principal stress space with the generators of the outer apices of the M–C hexagonal pyramids, we obtain the same relations.

An analogous set of transformations can be obtained if the D–P cone is made to coincide with the generators of the inner apices of the same M–C hexagonal pyramids in the principal stress space. In such a case, the D–P solid predicts the same behaviour as the M–C solid for the so-called extension test in which a decreasing axial stress follows the initially applied confining pressure. The material transformations between the M–C and D–P inner cones are given in the Appendix.

Material parameters were determined for Castlegate sandstone (a weak sandstone) using triaxial compression tests. It was found that the elastic constants are $E = 8{\cdot}1$ GPa and $\nu = 0{\cdot}35$. The angle of internal friction was found to be $\varphi = 32^\circ$ and an associated flow-rule, with the dilation angle $\psi = \varphi$, was assumed because the rock showed pronounced dilatancy. These values give $\bar{\eta} = \bar{\mu} = 3{\cdot}329$ for the M–C model. Figure 1 shows the variation of equivalent stress with equivalent plastic strain, as obtained from the triaxial compression tests, with three different confining pressures. The results of the test with confining pressure $p_0 = 10$ MPa were fitted with the relation of the type (69). For the M–C model we found the parameters $\bar{K} = 9{\cdot}589 \times 10^{-8}$, $\bar{Y} = 25$ MPa and $n = 3{\cdot}547$. The corresponding D–P outer cone parameters are $\mu = \eta = 1{\cdot}311$, $K = 1{\cdot}30 \times 10^{-6}$, $Y = 14{\cdot}08$ MPa and $n = 3{\cdot}547$. For the D–P inner cone we have $\mu = \eta = 0{\cdot}912$, $K = 6{\cdot}778 \times 10^{-6}$, $Y = 9{\cdot}80$ MPa and $n = 3{\cdot}547$. No attempt was made to incorporate post stress-peak data in the curve fitting procedure since the emergence of shear bands beyond the maximum equivalent stress is not accounted for in the present analysis. Also, because of diffuse

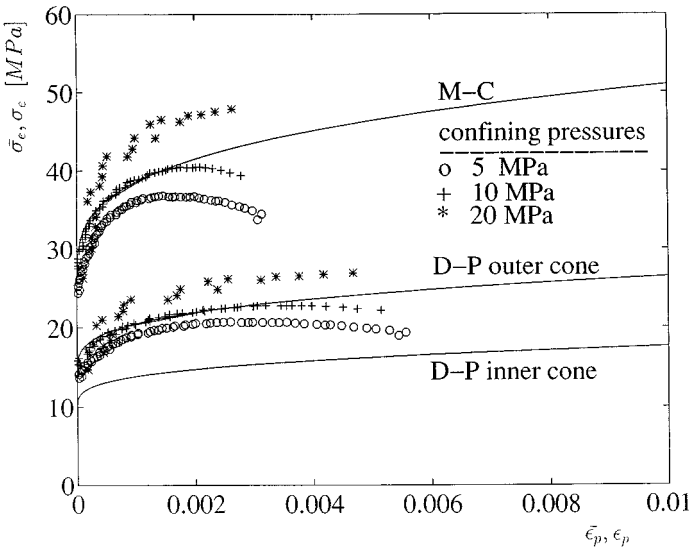

Figure 1. Castlegate sandstone triaxial compression tests. Equivalent stres ($\bar{\sigma}_e, \sigma_e$) vs. equivalent plastic strain ($\bar{\varepsilon}_p, \varepsilon_p$) for the M–C and D–P models at different confining pressures

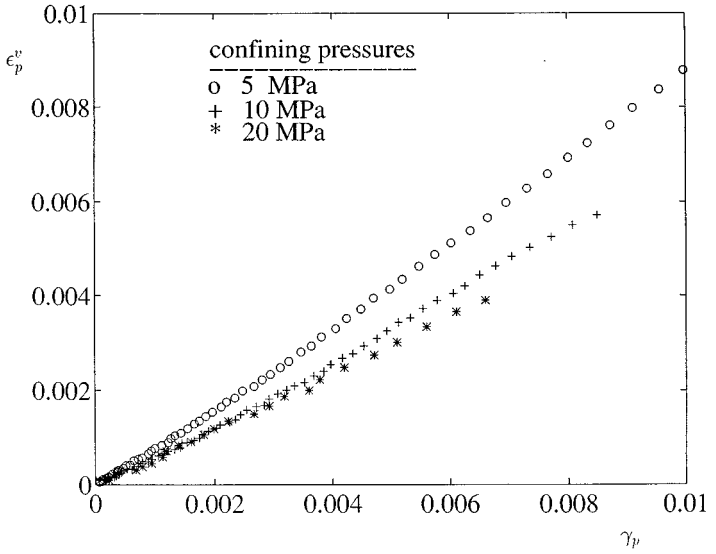

Figure 2. Volumetric plastic strain vs. shear plastic strain of Castlegate sandstone at different levels of confining pressure

and localized bifurcations, standard laboratory tests have the tendency to yield apparent values for the dilation angle which are unrealistic and occasionally not physically meaningful. This is shown in Figure 2 where the volumetric plastic strain $\varepsilon_{\mathrm{p}}^{\mathrm{v}} = \varepsilon_1^{\mathrm{p}} + 2\varepsilon_2^{\mathrm{p}}$ was plotted as a function of the shear plastic strain $\gamma_{\mathrm{p}} = 2\varepsilon_2^{\mathrm{p}} - \varepsilon_1^{\mathrm{p}}$. The slope of these curves gives the value of the dilation angle $\sin\psi$. We observed that while the dilation angle is more or less constant during each test it decreases with confining pressure. The value of the dilation angle at the low confining pressure test (5 MPa) is unrealistically high, whereas for the 20 MPa test the dilation angle is close to the friction angle.

A second set of material parameters were determined using data from fully drained triaxial compression tests on a Jurassic shale. The elastic constants are $E = 3{\cdot}7$ GPa and $\nu = 0{\cdot}35$. The angle of internal friction is $\varphi = 17^\circ$ and an associated flow-rule with the dilation angle $\psi = \varphi$ was assumed. These values give $\bar{\mu} = \bar{\eta} = 1{\cdot}826$ for the Mohr–Coulomb model. The calibration of the effective stress $\bar{\sigma}_{\mathrm{e}}$ as a function of plastic strain is given by (69) where $\bar{Y} = 15$ MPa, $\bar{K} = 6{\cdot}278 \times 10^{-7}$ MPa and $n = 2{\cdot}857$. The associated D–P parameters were calculated from the transformation formulae.

5. RESULTS

As a first example, we have modelled the deformation of a thick-walled cylinder of Castlegate sandstone under increasing external pressure. This test is usually used to simulate the deformation and assess the failure of a wellbore during drilling. The experiments were performed with a thick-walled cylinder of internal radius $a = 0{\cdot}5$ cm and a ratio of external to internal radius $b/a = 5$, under plane-strain conditions. Figure 3 shows the hole closure versus external pressure curve of the thick-walled cylinder for two tests with different internal pressure, $p_0 = 2$ MPa and $p_0 = 10$ MPa. The initial part of the curve is almost linear, although due to the stress concentration, initial yielding at the borehole wall takes place quite early. The theoretical predictions obtained from the M–C and D–P inner cone models agree with experimental data. The slight

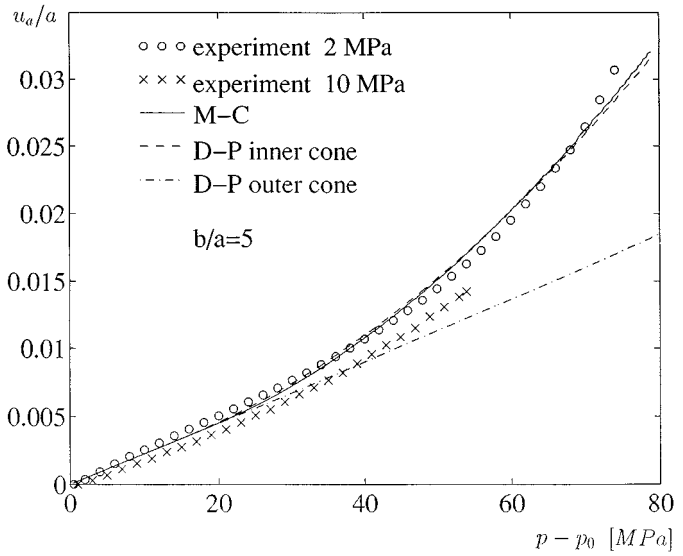

Figure 3. Castlegate sandstone hollow cylinder ($b/a = 5$) under increasing external pressure p. The radial displacement at the cavity is $u_a = -u(r = a)$

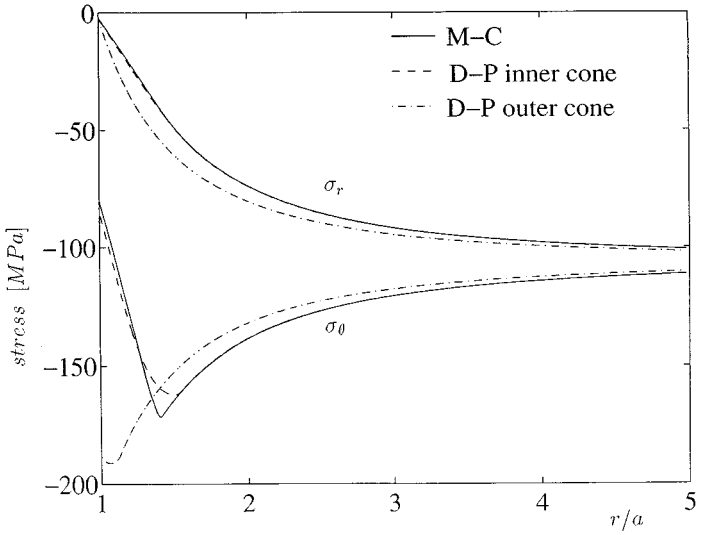

Figure 4. Radial profiles of polar stress components in the thick-walled cylinder of Castlegate sandstone for the case of $p_0 = 2$ MPa and $p = 100$ MPa

deviation from the experimental data at higher load may be due to the onset of localization of deformation. By comparison, the D–P outer cone model exhibits a stiffer behaviour: apparently since the stress path is within a range in the stress space where the M–C pyramid is fairly close to the D–P inner cone, while the D–P outer cone is at a considerable distance from the actual stress path. Figure 4 shows the radial stress profiles in the thick-walled cylinder subjected to an internal

pressure of $p_0 = 2$ MPa and an external pressure of $p = 100$ MPa. It may be concluded from Figure 4 that the D–P inner cone model gives results which are almost identical to those obtained from the M–C theory. The D–P outer cone predictions are considerably different near the cavity.

We have also examined the problem of an internally pressurized cavity embedded in an infinite medium of Jurassic shale. Figure 5 depicts the hole expansion versus internal pressure obtained with the three models. A similar picture is revealed for the stress profiles of an internally pressurized cavity with $p = 80$ MPa (Figure 6); the remote stress-field is 20 MPa. Once more, the

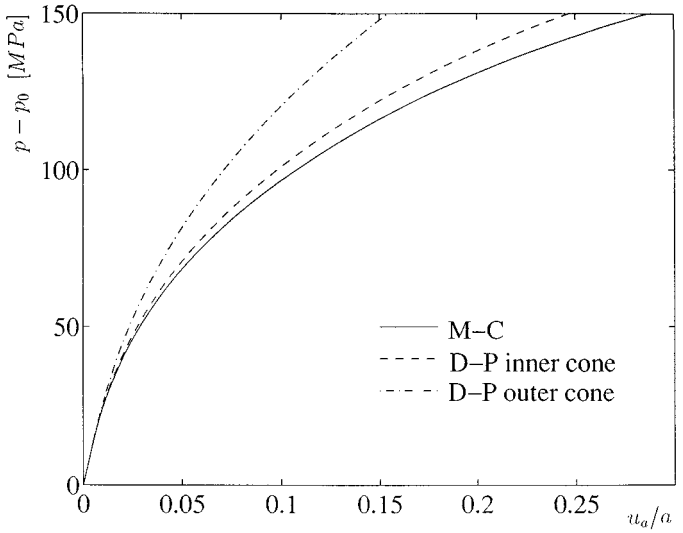

Figure 5. Internal pressure vs. cavity expansion of cylinderical cavity embedded in an infinite medium of Jurassic shale, $p_0 = 20$ MPa

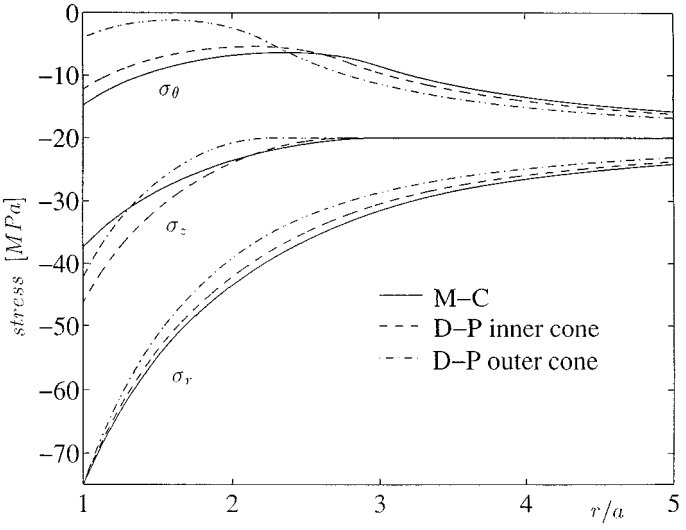

Figure 6. Radial profiles of stress components for the internally pressurized cylindrical cavity embedded in Juraic shale for $p_0 = 20$ MPa and $p = 80$ MPa

D–P inner cone model gives results which are close to those obtained from the M–C. Notice however that both D–P models predict axial stresses which differ from the M–C results in the plastic zone.

Sensitivity of the results to material parameters, like friction and dilation angles, is provided for the case of a cavity subjected to internal pressure in terms of limit pressure predictions. Material behaviour is described by the M–C relation (69) with parameters $E = 10{,}000$ MPa, $\nu = 0{\cdot}3$, $\bar{\mu} = \bar{\eta} = 3$, $\bar{K} = 10^{-7}$, $\bar{Y} = 25$ MPa and $n = 3{\cdot}5$. The associated D–P constants were calculated from the transformation formulae. Values of the limit pressure in the internally pressurized cavity problem are illustrated by the first three cases of Table I for associated models but with different values of parameters $\bar{\mu} = \bar{\eta}$. The other material constants remain as before. For $\bar{\mu} = \bar{\eta} = 1$ the two D–P models become identical with the Mises solid while the M–C model then agrees with the Tresca material. This observation was used to compare the results of the present analysis with those of Durban[6] for the Mises solid. With increasing values of $\bar{\mu} = \bar{\eta}$ the D–P inner cone model gives results which approach those obtained from the M–C model, while the outer D–P cone is predicting much higher values of internal pressure. The strengthening effect of the outer D–P cone model is now apparent. Also, higher values of $\bar{\mu} = \bar{\eta}$ increase the plastic strength of the material.

The effect of non-associativity, in the internally pressurized cavity, has been examined in cases 1, 4 and 5 of Table I which were obtained with a fixed value of $\bar{\mu} = 3$ and different levels of dilation $\bar{\eta}$ (other material parameters remained the same as before). It can be seen that increasing the level of non-associativity, by decreasing $\bar{\eta}$ with a constant value of $\bar{\mu}$, predicts weaker material response. Similar observations with regard to the influence of parameters $\bar{\mu}, \bar{\eta}$ in the pressurized cylindrical cavity problem are reported in earlier work by Carter *et al.*,[1] Bigoni and Laudiero,[2] Yu and Houlsby[3] and Durban and Fleck[8] for the related problem of a pressurized spherical cavity.

Finally, we obtained the limit pressure for an elastic/perfectly plastic material by neglecting the strain hardening of the M–C model upon assuming a large value for $\bar{K}$ in (69). The results are shown in Table II in comparison with the limit pressure calculated with a formula of the type

Table I. Limit pressures (in MPa) for a hardening material

Case	$\bar{\mu}$	$\bar{\eta}$	M–C	D–P inner cone	D–P outer cone
1	3	3	467	467	1092
2	2	2	327	350	542
3	1	1	192	222	222
4	3	2	368	378	744
5	3	1	216	222	334

Table II. Limit pressures (in MPa) for an elastic/perfectly plastic M–C material

Case	$\bar{\mu}$	$\bar{\eta}$	Present analysis	Carter *et al.*[1]
1	3	3	337	332
2	2	2	199	197
3	1	1	81	80
4	3	2	250	248
5	3	1	131	130

suggested by Carter *et al.*[1] Our results are slightly higher than the predictions by Carter *et al.*[1] The small difference may be due to the large-strain analysis whereas the results by Carter *et al.* were obtained using a small-strain analysis.

6. CONCLUSIONS

A large-strain elastoplastic analysis for problems of cylindrical cavity expansion and contraction in an infinite medium has been presented. The analysis employs non-associated deformation-type theories for Mohr–Coulomb and Drucker–Prager hardening solids. Of course, the flow theory models can be used to solve axially symmetric problems with large strains by applying an incremental step-by-step integration scheme. It is expected however that the present deformation theories will predict results similar to those obtained from the flow theories. Sample calculations have indeed verified that the loading paths are nearly proportional (recall that the associated M–C flow theory equations are holonomic).

We found that the material models predict, with good accuracy, the primary response of the thick-walled cylinder experiment, and we have examined the sensitivity of the results to friction and dilation angles for the problem of limit pressure in cavity expansion. Important applications of the present paper are validations of available numerical codes and reduction to the more simplified small-strain solutions. Strain softening can easily be implemented in this analysis by replacing the equivalent stress with the equivalent plastic strain as the independent variable. Primary equilibrium paths are also essential for assessing the possibility of bifurcations away from the axially symmetric patterns.

ACKNOWLEDGEMENTS

The authors are grateful to J. Cook of SCR for providing the experimental data. Part of this study was supported by the fund for the promotion of research at the Technion.

APPENDIX

Material parameters transformation from M–C to D–P inner cone

$$\bar{\eta} = \frac{1 + \frac{1}{3}\eta}{1 - \frac{2}{3}\eta} \;\Leftrightarrow\; \eta = \frac{3(\bar{\eta} - 1)}{2\bar{\eta} + 1} \tag{72}$$

$$\bar{\mu} = \frac{1 + \frac{1}{3}\mu}{1 - \frac{2}{3}\mu} \;\Leftrightarrow\; \mu = \frac{3(\bar{\mu} - 1)}{2\bar{\mu} + 1} = \frac{6\sin\varphi}{3 + \sin\varphi} \tag{73}$$

$$\phi = (1 - \tfrac{2}{3}\eta)\bar{\phi}, \quad \sigma_e = (1 - \tfrac{2}{3}\mu)\bar{\sigma}_e = \frac{3(1 - \sin\varphi)}{3 + \sin\varphi}\,\bar{\sigma}_e \tag{74}$$

$$\varepsilon^p = \frac{\bar{\varepsilon}^p}{1 - \frac{2}{3}\mu} \tag{75}$$

$$K = \frac{\bar{K}}{(1 - \frac{2}{3}\mu)^{n+1}}, \quad Y = (1 - \tfrac{2}{3}\mu)\,\bar{Y} \tag{76}$$

REFERENCES

1. J. P. Carter, J. R. Booker and S. K. Yeung, 'Cavity expansion in cohesive frictional soils', *Géotechnique*, **36,** 349–358 (1986).
2. D. Bigoni and F. Laudiero, 'The quasi-static finite expansion in a non-standard elasto-plastic medium', *Int. J. Mech. Sci.*, **21,** 825–837 (1989).
3. H. S. Yu and G. T. Houlsby, 'Finite cavity expansion in dilatant soils: loading analysis', *Géotechnique*, **41,** 173–183 (1991).
4. E. Detournay, 'Elastoplastic model of a deep tunnel for a rock with a variable dilatancy', *Mech. Rock Eng.*, **19,** 99–108 (1986).
5. I. F. Collins and J. R. Stimpson, 'Similarity solutions for drained and undrained cavity expansions in soils', *Géotechnique*, **44,** 21–34 (1994).
6. D. Durban, 'Finite straining of pressurized compressible elasto-plastic tubes', *Int. J. Eng. Sci.*, **26,** 939–950 (1988).
7. D. Durban and M. Kubi, 'A general solution for the pressurized elastoplastic tube', *J. appl Mech.*, **59,** 20–26 (1992).
8. D. Durban and N. A. Fleck, 'Spherical cavity expansion in a Drucker–Prager solid', *J. appl. Mech.* (to appear).
9. D. C. Drucker and W. Prager, 'Soil mechanics and plastic analysis or limit design', *Q. Appl. Math.*, **12,** 157–165 (1952).